Check for updates

JGR Space Physics

RESEARCH ARTICLE
10.1029/2021JA029156

Key Points:

- Midtail foreshock transients develop under mostly similar formation conditions as dayside ones
- Almost all midtail foreshock transients have electron heating which is proportional to the solar wind speed
- Foreshock transients may be stable for tens of minutes and continuously disturb the local bow shock and accelerate particles

Supporting Information:

Supporting Information may be found in the online version of this article.

Correspondence to:

T. Z. Liu,
terryliuzixu@ucla.edu

Citation:

Liu, T. Z., Zhang, H., Wang, C.-P., Angelopoulos, V., Vu, A., Wang, X., & Lin, Y. (2021). Statistical study of foreshock transients in the midtail foreshock. *Journal of Geophysical Research: Space Physics*, *126*, e2021JA029156. https://doi.org/10.1029/2021JA029156

Received 20 JAN 2021
Accepted 9 APR 2021

© 2021. American Geophysical Union. All Rights Reserved.

Statistical Study of Foreshock Transients in the Midtail Foreshock

Terry Z. Liu[1,2], Hui Zhang[2], Chih-Ping Wang[3], Vassilis Angelopoulos[4], Andrew Vu[2], Xueyi Wang[5], and Yu Lin[5]

[1]Cooperative Programs for the Advancement of Earth System Science, University Corporation for Atmospheric Research, Boulder, CO, USA, [2]Geophysical Institute, University of Alaska, Fairbanks, Fairbanks, AK, USA, [3]Department of Atmospheric and Oceanic Sciences, University of California, Los Angeles, Los Angeles, CA, USA, [4]Department of Earth, Planetary, and Space Sciences, University of California, Los Angeles, Los Angeles, CA, USA, [5]Physics Department, Auburn University, Auburn, AL, USA

Abstract In the dayside foreshock, many foreshock transients have been observed and simulated. Because of their strong dynamic pressure perturbations, foreshock transients can disturb the local bow shock, magnetosheath, magnetopause, and thus the magnetosphere-ionosphere system. They can also accelerate particles contributing to shock acceleration. Recent observations and simulations showed that foreshock transients also exist in the midtail foreshock, which can continuously disturb the nightside bow shock, magnetosheath, and magnetopause while propagating tailward for tens of minutes. To further understand the characteristics of midtail foreshock transients, we studied them statistically using Acceleration Reconnection Turbulence & Electrodynamics of Moon's Interaction with the Sun observations. We selected 111 events that have dynamic pressure decrease along the local bow shock normal by more than 50%. We show that the dynamic pressure decrease is contributed by both density decrease and speed decrease. Around 90% of the events have electron temperature increase by more than 10% with a temperature change ratio proportional to the solar wind speed. Midtail foreshock transients more likely occur at the dawnside than the duskside. They are more significant closer to the bow shock and rather stable along the tailward direction. They have similar formation conditions compared to the dayside foreshock transients, except the ones related to the bow shock geometry. Our study indicates that the characteristics of foreshock transients based on dayside observations need to be generalized. Our study also implies that foreshock transients can exist for tens of minutes (even longer for larger planar shocks), continuously disturbing the local shock and accelerating/heating particles.

1. Introduction

In the dayside foreshock (e.g., Eastwood et al., 2005), many foreshock transients have been observed and simulated, for example, hot flow anomalies (e.g., Lin, 1997, 2002; Omidi & Sibeck, 2007; Schwartz et al., 2018, 1985; Zhang, Sibeck, Zong, Gary, et al., 2010), spontaneous hot flow anomalies (SHFAs) (Omidi, Zhang, et al., 2013; Zhang, Sibeck, Zong, Omidi, et al., 2013), foreshock bubbles (FBs) (e.g., Z. Liu et al., 2015; Omidi et al., 2010, 2020; Turner et al., 2020, 2013), foreshock cavitons (e.g., Blanco-Cano et al., 2009, 2011), and foreshock cavities (e.g., Omidi, Sibeck, et al., 2013; Sibeck, Phan, et al., 2002). These types of foreshock transients have a core region with low density, and HFAs, SHFAs, and FBs also have significant velocity deflection within the core, resulting in low dynamic pressure. As a result, when they encounter the bow shock, the local bow shock will move outward. Such perturbations can propagate into the magnetosheath and disturb the magnetopause and thus magnetosphere-ionosphere system (e.g., Archer et al., 2014, 2015; Shen et al., 2018; Sibeck, Borodkova, et al., 1999; Turner, Eriksson, et al., 2011; B. Wang et al., 2018, 2020; Zhao et al., 2017a).

Foreshock transients can also accelerate particles (e.g., Kis et al., 2013; T. Z. Liu et al., 2017a; Wilson et al., 2016, 2013). For example, as the boundary of foreshock transients convects toward the bow shock, particles can bounce between the shock and that boundary and gain energy through Fermi acceleration (Liu et al., 2017b, 2018; Turner, Wilson, et al., 2018). During the expansion of foreshock transients, the outward transport of magnetic flux can accelerate electrons through betatron acceleration (Liu et al., 2019, 2020a). If the expansion of foreshock transients is supermagnetosonic, a shock can form, which can reflect and

21699402, 2021, 5, Downloaded from https://agupubs.onlinelibrary.wiley.com/doi/10.1029/2021JA029156 by Auburn University Libraries, Wiley Online Library on [08/11/2022]. See the Terms and Conditions (https://onlinelibrary.wiley.com/terms-and-conditions) on Wiley Online Library for rules of use; OA articles are governed by the applicable Creative Commons License

accelerate solar wind particles through shock drift acceleration (T. Z. Liu et al., 2016a). Inside foreshock transients, magnetic reconnection has also been observed to energize electrons (T. Z. Liu et al., 2020b; S. Wang, Chen, et al., 2020). These studies indicate that foreshock transients can contribute to particle acceleration at shocks.

Recent studies showed that foreshock transients occur not only in the dayside foreshock but also in the midtail foreshock at $X \sim -30$ to -50 R_E. Using multiple spacecraft, C.-P. Wang, Liu, et al. (2018) found that foreshock transient-driven perturbations in the magnetosheath can propagate with the driver solar wind discontinuity from dayside to midtail, causing the midtail magnetopause to locally move outward. Using STEREO observations, Facskó, Opitz, et al. (2015) also found HFA-like perturbations in the far tail magnetosheath ($X \sim -310$ R_E). Using Acceleration Reconnection Turbulence & Electrodynamics of Moon's Interaction with the Sun (ARTEMIS) observations, T. Z. Liu et al. (2020c) identified foreshock transients in the midtail foreshock. In global hybrid simulations by C.-P.Wang, Wang, et al. (2020), an FB generated in the dayside foreshock propagated with its driver solar wind discontinuity to the midtail foreshock. These results indicate that as foreshock transients propagate tailward, they continuously disturb the local nightside bow shock, magnetosheath, and magnetopause for tens of minutes.

To further understand the properties and formation conditions of midtail foreshock transients, we conducted a statistical study using ARTEMIS observations. We selected 111 events that have dynamic pressure decrease by more than 50%. The data and event selection details are introduced in Section 2. We present a case study in Section 3.1. We show the statistical properties and formation conditions of midtail foreshock transients in Sections 3.2 and 3.3, respectively. We conclude and discuss our results in Section 4.

2. Data and Methods

We used data from the two ARTEMIS spacecraft at lunar orbit from 2010 to 2019, which were part of Time History of Events and Macroscale Interactions during Substorms (THEMIS, Angelopoulos, 2008) before 2010 (TH-B and TH-C, respectively). We analyzed plasma data from the electrostatic analyzer (McFadden et al., 2008) and magnetic field data from the fluxgate magnetometer (Auster et al., 2008). We used OMNI data from 2010 to 2019 to obtain the properties of background solar wind. For the properties of background solar wind discontinuities, we used TH-B data in the solar wind from 2010 to 2019 and applied normalized partial variance of increments (PVI > 5) to identify discontinuities (e.g., Greco et al., 2008).

Every month the two ARTEMIS spacecraft crossed the midtail bow shock twice. By checking the bow shock crossings from 2010 to 2019, we identified more than 200 foreshock transients by eye, including HFAs, SHFAs, FBs, foreshock cavitons, and foreshock cavities (T. Z. Liu et al., 2020c). For each event, we manually selected the time intervals of the background before and after the event so that other foreshock transients, solar wind discontinuities, and bow shock crossings can be excluded. We then obtained the average density, magnetic field, velocity, and electron temperature (ion temperature is not measured correctly in the solar wind/foreshock) in the pre-transient and post-transient background. Using these solar wind parameters, we calculated the local bow shock normal using the bow shock model by Merka et al. (2005). We also manually selected the time interval of the core region to obtain the minimum density, minimum field strength, minimum speed along the local bow shock normal, minimum dynamic pressure along the local bow shock normal, and maximum electron temperature within the core. For each quantity, we calculated both the ratio to the pre-transient background and the ratio to the post-transient background and chose the one that exhibits greater variation for further analysis. Because we only want to focus on those foreshock transients that are significant enough to disturb the bow shock, we required that the dynamic pressure along the local bow shock normal inside foreshock transients should decrease by more than 50%, and thus a total of 111 events were selected (see Table S1 in the supporting information).

The two ARTEMIS spacecraft were typically separated by a few R_E. When one spacecraft observed an event, the other spacecraft either was further upstream, observed the same event or its bow shock response, or was in the magnetosheath. For the statistical study, we only used data from one spacecraft. If both spacecraft observed an event, we chose the one with the more significant variation of quantities. An example of midtail foreshock transients is shown in the next section.

21699402, 2021, 5, Downloaded from https://agupubs.onlinelibrary.wiley.com/doi/10.1029/2021JA029156 by Auburn University Libraries, Wiley Online Library on [08/11/2022]. See the Terms and Conditions (https://onlinelibrary.wiley.com/terms-and-conditions) on Wiley Online Library for rules of use; OA articles are governed by the applicable Creative Commons License

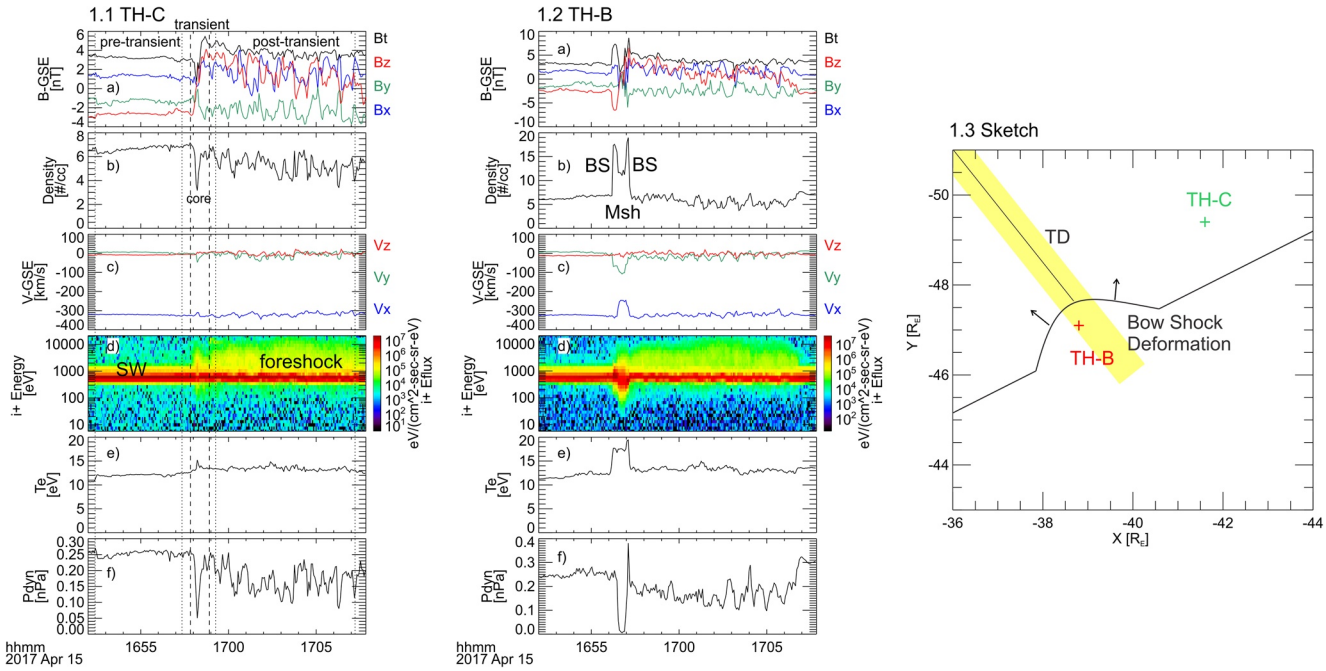

Figure 1. TH-C (1.1) and TH-B (1.2) observations of a midtail foreshock transient. Figures 1.1 and 1.2 from top to bottom are magnetic field in GSE, density, velocity in GSE, ion energy spectrum, electron temperature, and dynamic pressure along the local bow shock normal. SW, Msh, and BS are short for "solar wind", "magnetosheath", and "bow shock", respectively. Figure 1.3 is a sketch showing that as the observed foreshock transient propagated tailward with the tangential discontinuity, the local bow shock (from the Merka et al. (2005) model) moved outward with perturbations in the local magnetosheath. The black arrows indicate the local bow shock normal crossed by TH-B.

3. Results

3.1. Case Study

In this example, TH-C was at [-41.6, −49.4, 5.2] R_E in GSE, initially in the solar wind (Figure 1.1d). Because of a solar wind discontinuity at ~16:58 UT, TH-C entered the foreshock region characterized by the presence of foreshock ions (Figure 1.1d) and ultralow frequency waves (Figure 1.1a). At the discontinuity, there was a foreshock transient that had a core with low field strength (Figure 1.1a), low density (Figure 1.1b), moderate velocity variation (Figure 1.1c), and moderate plasma heating (Figure 1.1e). The time intervals of the core region and background are labeled as vertical dashed and dotted lines, respectively. By assuming that the discontinuity was a tangential discontinuity (TD), we calculated the TD normal as [0.78, 0.62, 0.06] in GSE using the cross product method (Schwartz, 1998). Thus, the transient could be a weak HFA driven by the TD. To estimate the local bow shock normal from the Merka et al. (2005) model, we used the field strength, density, and velocity averaged between the pre-transient and post-transient background and obtained [0.45, −0.89, 0.08] in GSE (see sketch in Figure 1.3). We then calculated the dynamic pressure along the local bow shock normal shown in Figure 1.1f. It decreased from ~0.25 nPa in the background to ~0.05 nPa in the core due to both the density decrease and speed decrease along the bow shock normal (in +*X* and -*Y* direction).

TH-B was several R_E closer to the bow shock at [−38.8, −47.1, 5.5] R_E in GSE (also see sketch in Figure 1.3). TH-B also observed the transition from the solar wind to the foreshock caused by the solar wind discontinuity (Figure 1.2). At the discontinuity, possibly due to the dynamic pressure decrease inside the foreshock transient, the bow shock moved outward causing TH-B to temporarily enter the magnetosheath (seen from the high density) and cross the bow shock twice. Using the mixed-mode coplanarity method (Schwartz, 1998), we calculated that the bow shock normal of first and second crossings was [−0.09, −0.99, −0.00] and [0.77, −0.62, −0.12] in GSE, respectively (black arrows in Figure 1.3). Such a bow shock geometry led to a bulge (Figure 1.3) consistent with the local outward motion. Inside the magnetosheath, TH-B also observed a core-like structure with low density and low field strength likely corresponding to the foreshock transient perturbation. Such bow shock and magnetosheath disturbances are consistent with

21699402, 2021, 5, Downloaded from https://agupubs.onlinelibrary.wiley.com/doi/10.1029/2021JA029156 by Auburn University Libraries, Wiley Online Library on [08/11/2022]. See the Terms and Conditions (https://onlinelibrary.wiley.com/terms-and-conditions) on Wiley Online Library for rules of use; OA articles are governed by the applicable Creative Commons License

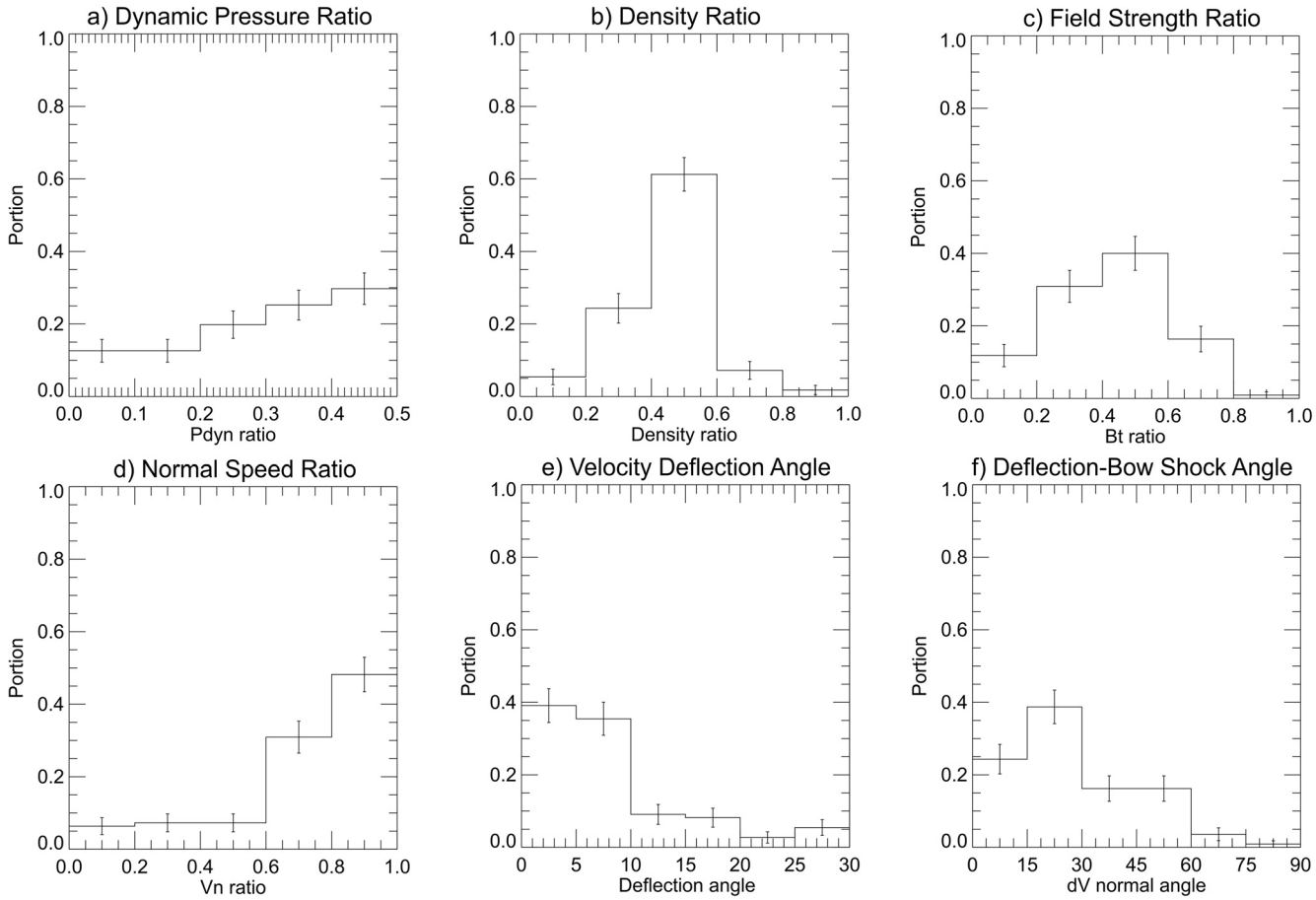

Figure 2. The probability distribution of the minimum ratio of parameters in the core to the background: (a) dynamic pressure along the local bow shock normal; (b) density; (c) magnetic field strength; (d) speed along the local bow shock normal (normal speed V_n). And the probability distribution of (e) the maximum angle between the velocity in the core and in the background and (f) the minimum angle between the deflected velocity dV and the local bow shock normal. The error bars are calculated based on binomial distributions.

case studies by T. Z. Liu et al. (2020c). Because of their dynamic perturbations (Figure 1.1f) and plasma heating (Figure 1.1e), it is necessary to examine the statistical characteristics of midtail foreshock transients shown in Sections 3.2 and 3.3.

3.2. Properties

Figure 2a shows the probability distribution of the minimum ratio of dynamic pressure along the local bow shock normal within the core to that in the background. As can be seen from the trend, there should be more events with dynamic pressure ratio above 50%, but because those events may not be significant enough to greatly disturb the bow shock, they are excluded as mentioned in Section 2. To investigate the contribution of the density decrease to the dynamic pressure decrease, Figure 2b shows the probability distribution of the minimum density ratio. The majority of events have a ratio between 20% and 60%, with a peak at around 50%, possibly due to our selection criterion on the dynamic pressure decrease to be at least 50%. The probability distribution of the minimum magnetic field strength ratio (Figure 2c) shows a similar profile (also see the case study in Figures 1.1a and 1.1b) but is less concentrated between 20% and 60% compared to the density ratio.

To investigate the contribution of the velocity deflection and deceleration to the dynamic pressure decrease, Figure 2d shows the minimum ratio of speed along the local bow shock normal (normal speed). Around half of the events have weak deflection and deceleration with a ratio above 80%, which could be foreshock cavities and foreshock cavitons. Around 30% of events have clear deflection and deceleration with a ratio

21699402, 2021, 5, Downloaded from https://agupubs.onlinelibrary.wiley.com/doi/10.1029/2021JA029156 by Auburn University Libraries, Wiley Online Library on [08/11/2022]. See the Terms and Conditions (https://onlinelibrary.wiley.com/terms-and-conditions) on Wiley Online Library for rules of use; OA articles are governed by the applicable Creative Commons License

21699402, 2021, 5, Downloaded from https://agupubs.onlinelibrary.wiley.com/doi/10.1029/2021JA029156 by Auburn University Libraries, Wiley Online Library on [08/11/2022]. See the Terms and Conditions (https://onlinelibrary.wiley.com/terms-and-conditions) on Wiley Online Library for rules of use; OA articles are governed by the applicable Creative Commons License

between 60% and 80%, and a few events have very strong deflection and deceleration with a ratio less than 60%. These events are likely HFAs, FBs, and SHFAs with deflection and deceleration that can significantly contribute to the dynamic pressure decrease. Figure 2e shows the probability distribution of the maximum angle between the velocity in the core and in the background (i.e., deflection angle). Because the midtail bow shock is very tilted (by ∼60° compared to the nose, e.g., as in the case study in Section 3.1), the speed decrease along the local bow shock normal is only a small portion of the total bulk velocity. As a result, the maximum deflection angle is around 30° due to the bow shock geometry, and the majority of velocity deflection angles are within 10° corresponding to the normal speed ratio above 60% in Figure 2d. Figure 2f shows the probability distribution of the minimum angle between the deflected velocity (velocity difference between the core and background) and the local bow shock normal. The majority are within 60° and all the events are within 90°. This is consistent with a statistical study by S. Wang et al. (2013a) for dayside HFAs that the deflection direction is mainly away from the bow shock. This is because the velocity deflection is mainly due to the presence of foreshock ions and the outward expansion of foreshock transients (e.g., T. Z. Liu et al., 2020a). Note that this result is partially affected by our selection criterion as deflection toward the bow shock is less likely to cause a dynamic pressure decrease of more than 50% along the bow shock normal.

To examine whether the solar wind speed can affect the dynamic pressure depletion, we present in Figure 3a the relationship between the solar wind speed and the dynamic pressure ratio. There are fewer events with dynamic pressure ratio larger than ∼35% when the solar wind speed is above ∼500 km/s, suggesting that fast solar wind could more likely result in large dynamic pressure depletion. Figure 3b shows that there is no correlation between the solar wind speed and the density ratio. Figure 3c shows that there is a weak negative trend between the solar wind speed and the normal speed ratio, which is likely the reason for the trend in Figure 3a. Figure 3d shows that the field strength ratio likely has a weak tendency to decrease with increasing solar wind speed, which is different from the aforementioned density ratio trend.

As for electron heating, Figure 4a shows the probability distribution of the maximum electron temperature ratio. The majority of events have a ratio larger than 1.1, consistent with a statistical study by T. Z. Liu et al. (2017a) for dayside foreshock transients which showed that almost all foreshock transients can energize electrons in their core. Figure 4b shows that faster solar wind can lead to stronger electron heating, also consistent with T. Z. Liu et al. (2017a).

Figures 5a and 5b show the spatial distribution of foreshock transients, and the colors indicate the dynamic pressure ratio and electron temperature ratio, respectively. We see that there are more events on the dawnside (67.6%, 75 out of 111 events) than on the duskside (32.4%, 36 out of 111 events), consistent with the Parker spiral IMF configuration which causes the dawnside bow shock to be more likely quasi-parallel than the duskside bow shock. Additionally, the dynamic pressure ratio and the electron temperature ratio do not show a clear dependence on the tailward distance along the bow shock surface. As the midtail bow shock normal does not vary very much along the tailward direction, there could be self-similar background foreshock conditions. If foreshock transients dissipate/grow during their tailward propagation in the midtail foreshock, spacecraft further downtail should statistically observe weaker/stronger perturbations, but there is no clear trend in Figures 5a and 5b. It is possible that there is a mixture of dissipating, growing, and stable events. A case study by T. Z. Liu et al. (2020c) showed that an HFA was in a balanced state without expansion or contraction, and its maximum dynamic pressure decrease was nearly the same during its tailward propagation.

Furthermore, for each event, we calculated the distance between the spacecraft and the model bow shock (Merka et al., 2005) along the shock normal direction. We then separated the events into two groups based on the distance: an event is in the close to (far from) the bow shock group if the distance is negative (positive) (note that the separation is rather qualitative as the uncertainty of model bow shock is especially large in the midtail. See Figure S1 in the supporting information for more details). Figures 5c and 5d show the comparison of the probability distribution of dynamic pressure ratio and electron temperature ratio between the two groups. We see that the foreshock transients close to the bow shock more likely have dynamic pressure ratios below 0.3 and electron temperature ratios around 1.4–2.2 (also see Figure S1). This is consistent with the case study by T. Z. Liu et al. (2020c) showing that the spacecraft closer to the bow shock observed overall more significant variation than the one farther away. Additionally, HFAs and SHFAs

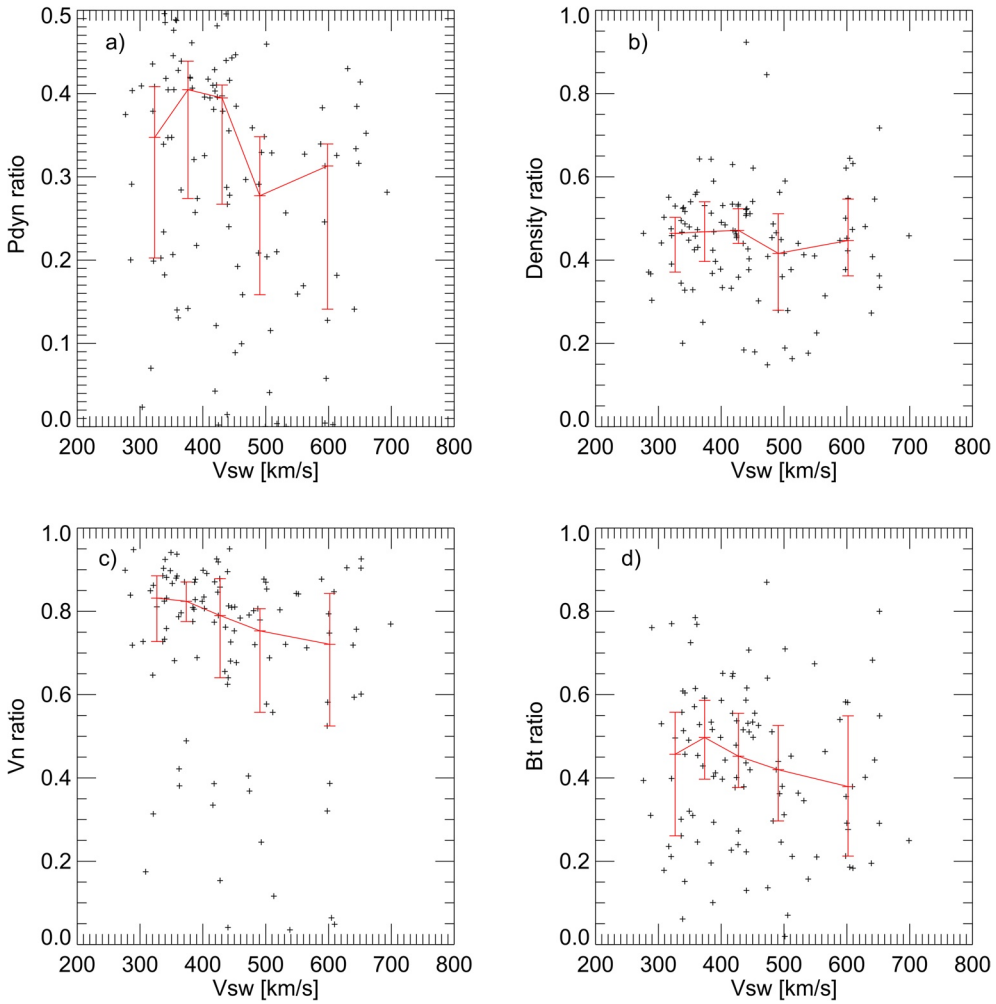

Figure 3. The dependence of the minimum ratio in the core to the background of (a) dynamic pressure along the local bow shock normal, (b) density, (c) speed along the local bow shock normal, and (d) field strength on the solar wind speed. The red bars indicate the median value, upper quartile (75%), and lower quartile (25%).

are typically close to the bow shock (e.g., Omidi & Sibeck, 2007; Omidi et al., 2013), and they can result in stronger dynamic pressure decrease and electron heating than foreshock cavities and foreshock cavitons that can be observed further upstream (e.g., Blanco-Cano et al., 2009; Omidi, Sibeck, et al., 2013) (see discussion about our foreshock transient categorization in Section 4).

We also found that there is a correlation between the dynamic pressure ratio and the electron temperature ratio with a correlation coefficient of −0.61 (Figure 5e). One possible explanation of this correlation is that the dynamic pressure decrease partially indicates the ion kinetic energy decrease compared to the background (except the part due to the relative motion between foreshock ions and solar wind ions). Thus, the energy source of electron heating could be related to the ion kinetic energy, consistent with PIC simulations by An et al. (2020) which demonstrated how the electric fields couple the energy among electrons, solar wind ions, and foreshock ions during the formation and evolution of foreshock transients.

3.3. Formation Conditions

Depending on different solar wind conditions, there can be multiple foreshock transient events within one hour or no events at all during one bow shock crossing (a few hours). To determine the solar wind conditions favorable for their formation, we used the probability distribution of the background solar wind parameters divided by the probability distribution of the same parameters obtained from 9 yr OMNI data

21699402, 2021, 5, Downloaded from https://agupubs.onlinelibrary.wiley.com/doi/10.1029/2021JA029156 by Auburn University Libraries, Wiley Online Library on [08/11/2022]. See the Terms and Conditions (https://onlinelibrary.wiley.com/terms-and-conditions) on Wiley Online Library for rules of use; OA articles are governed by the applicable Creative Commons License

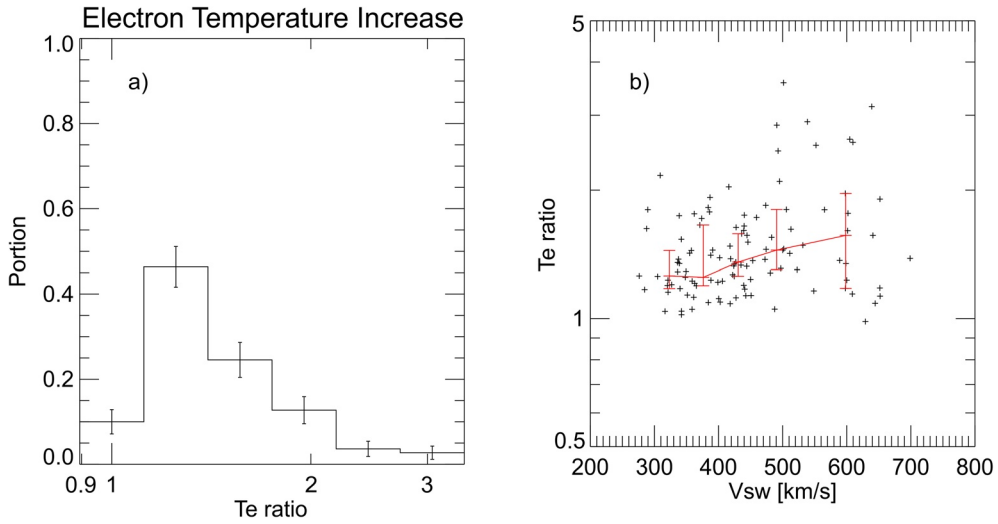

Figure 4. (a) The probability distribution of the maximum ratio of electron temperature in the core to the background. (b) The relationship between the electron temperature ratio and the solar wind speed. The red bars indicate the median value, upper quartile (75%), and lower quartile (25%).

(2010–2019). We used the average of the pre-transient and post-transient solar wind parameters as the estimate of the background solar wind values for each event. If the probability distribution ratio for a parameter within a certain range of values is larger than one, it means that this range represents a favorable formation condition. Figure 6a shows that midtail foreshock transients more likely occur at larger solar wind speed. This is consistent with statistical studies for dayside foreshock transients (Chu et al., 2017; Facskó, Németh, et al., 2009; Liu et al., 2017). Figure 6b shows that large solar wind Alfvén Mach number (M_A) favors the formation with a peak at ~10. Considering that the local bow shock is very tilted (by ~60°), the local bow shock M_A is nearly half of the solar wind M_A (see the probability distribution of local M_A in Figure S2 in the supporting information). Thus, the local M_A is overall smaller than that for the dayside events (Facskó, Németh, et al., 2009). But a bow shock M_A ~5 is still sufficient to form foreshock transients as shown in hybrid simulations (e.g., Lin, 2002; Omidi & Sibeck, 2007).

Figure 6c shows that low solar wind density is likely a favorable formation condition, though the observed correlation could be due to the inherent solar wind property that faster solar wind has a lower density. We thus plot the relationship between the solar wind density and the solar wind speed shown in Figure 7. We see that the relationship between these quantities for midtail foreshock transient events (Figure 7a) does not show a clear difference compared to that from OMNI data (Figure 7b), and the two plots are very similar to those for dayside foreshock transients by T. Z. Liu et al. (2017a). Between the two quantities, fast solar wind is more likely the favorable condition because fast solar wind can result in high foreshock ion speed, which favors the formation (e.g., An et al., 2020), whereas the solar wind density does not directly affect the bow shock and foreshock properties. Thus, we conclude that the observed anti-correlation of probability of formation of foreshock transients and reduced solar wind density in Figure 6c is mainly due to this speed-density anticorrelation in the solar wind.

Figure 6d shows that low IMF strength is also a favorable formation condition. To see whether this might also be due to an inherent solar wind property, we examine in Figure 7d the median value of the IMF strength as a function of solar wind speed. The figure shows that the IMF strength does not exhibit a correlation with solar wind speed. Additionally, Figure 7c shows that the IMF strength for our events is mostly below the median values in Figure 7d. The two plots are also very similar to those by T. Z. Liu et al. (2017a). The comparison between Figures 7c and 7d suggest that low IMF strength is indeed a favorable formation condition per Figure 6d.

The preference for low IMF strength and fast solar wind speed is consistent with the preference for high M_A, but because the fast solar wind has a low density (Figure 7b) and high minimum IMF strength (Figure 7d), the preference for M_A is not monotonic (Figure 6b). One possible explanation of such a non-monotonicity

21699402, 2021, 5, Downloaded from https://agupubs.onlinelibrary.wiley.com/doi/10.1029/2021JA029156 by Auburn University Libraries, Wiley Online Library on [08/11/2022]. See the Terms and Conditions (https://onlinelibrary.wiley.com/terms-and-conditions) on Wiley Online Library for rules of use; OA articles are governed by the applicable Creative Commons License

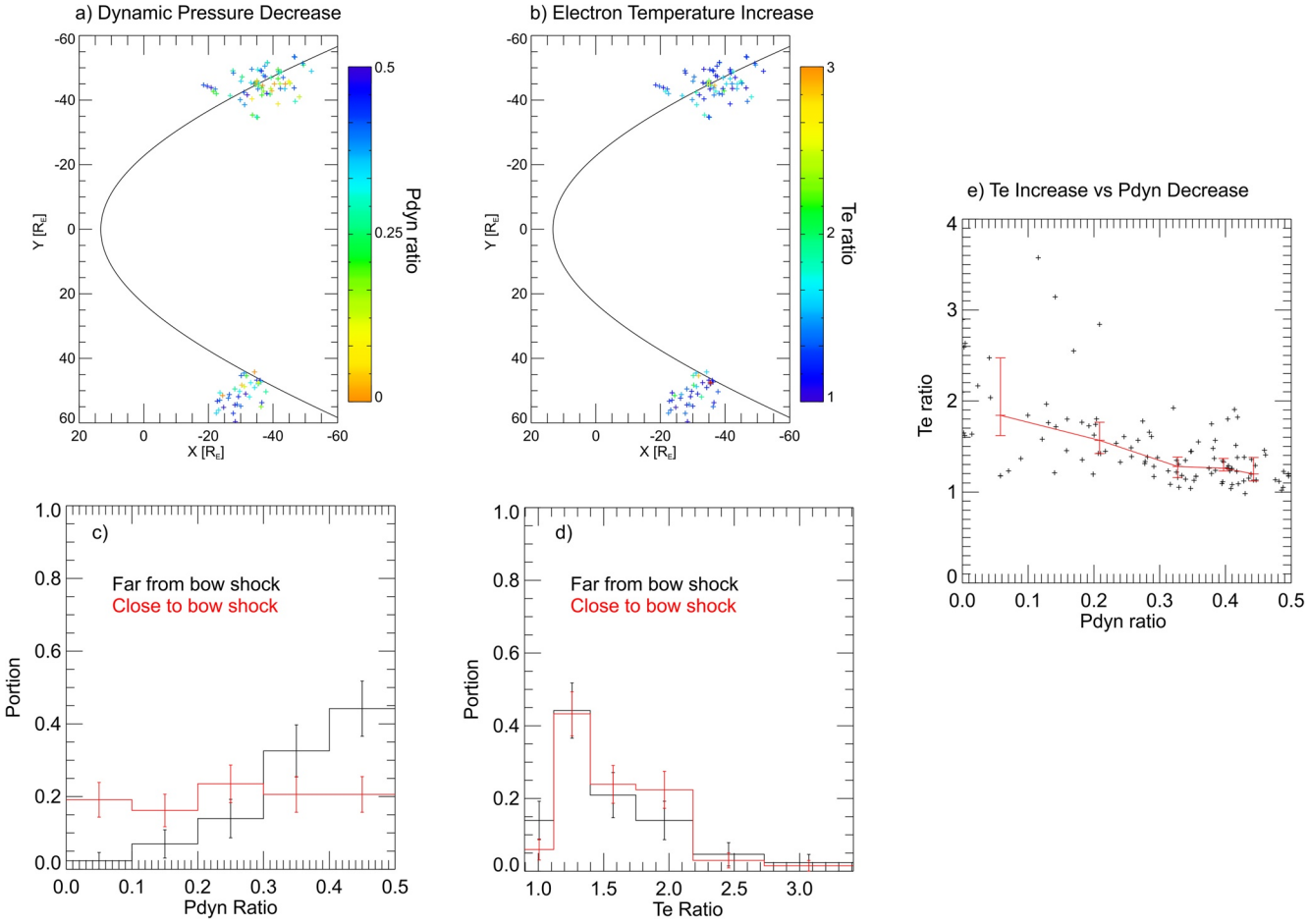

Figure 5. The spatial distribution of the foreshock transient events with colors indicating the dynamic pressure ratio (a) and electron temperature ratio (b). Brighter colors indicate larger dynamic pressure decrease along the local bow shock normal and larger electron temperature increase. The black curved lines are the sampled bow shock from the Merka et al. (2005) model. (c) The probability distribution of the minimum ratio in the core to the background of dynamic pressure along the local bow shock normal for events close to the bow shock (red) and far from the bow shock (black). (d) The probability distribution of the maximum ratio in the core to the background of electron temperature for events close to the bow shock (red) and far from the bow shock (black). (e) The relationship between the electron temperature ratio and the dynamic pressure ratio. The red bars indicate the median value, upper quartile (75%), and lower quartile (25%).

is that higher shock Mach number results in larger foreshock/solar wind ion density ratio, which favors the formation of foreshock transients. However, as the Mach number increases, this density ratio gradually saturates at ~20% (e.g., Paschmann & Sckopke, 1983).

Figures 6e and 6f show that there is no clear preference for IMF cone angles. This is different from dayside foreshock transients which preferentially occur under radial IMF conditions (e.g., Chu et al., 2017). The possible reason for the lack of a dependence of midtail transient formation on IMF cone angles is as follows: Around the bow shock nose, IMF cone angles are very close to the angle between the IMF direction and the bow shock normal (i.e., θ_{Bn}). Under radial IMF the bow shock is more likely quasi-parallel, which favors the formation of dayside foreshock transients. For the tilted midtail bow shock to generate the ion foreshock, however, there is no correlation between IMF cone angles and θ_{Bn} (see Figure S3, θ_{Bn} vs. cone angles and the probability distribution of θ_{Bn}).

We next examine the properties of the solar wind discontinuities. Figure 8a shows the probability distribution of the magnetic shear angle across the events normalized by that across the solar wind discontinuities. There is a trend that larger shear angles favor the formation of midtail foreshock transients. This is consistent with statistical studies for dayside HFAs (Facskó, Németh, et al., 2009; Schwartz et al., 2000; Zhao et al., 2017b), and the plot is very similar to that by Zhao et al. (2017b). There are 33 or 9 events (out of 111)

21699402, 2021, 5, Downloaded from https://agupubs.onlinelibrary.wiley.com/doi/10.1029/2021JA029156 by Auburn University Libraries, Wiley Online Library on [08/11/2022]. See the Terms and Conditions (https://onlinelibrary.wiley.com/terms-and-conditions) on Wiley Online Library for rules of use; OA articles are governed by the applicable Creative Commons License

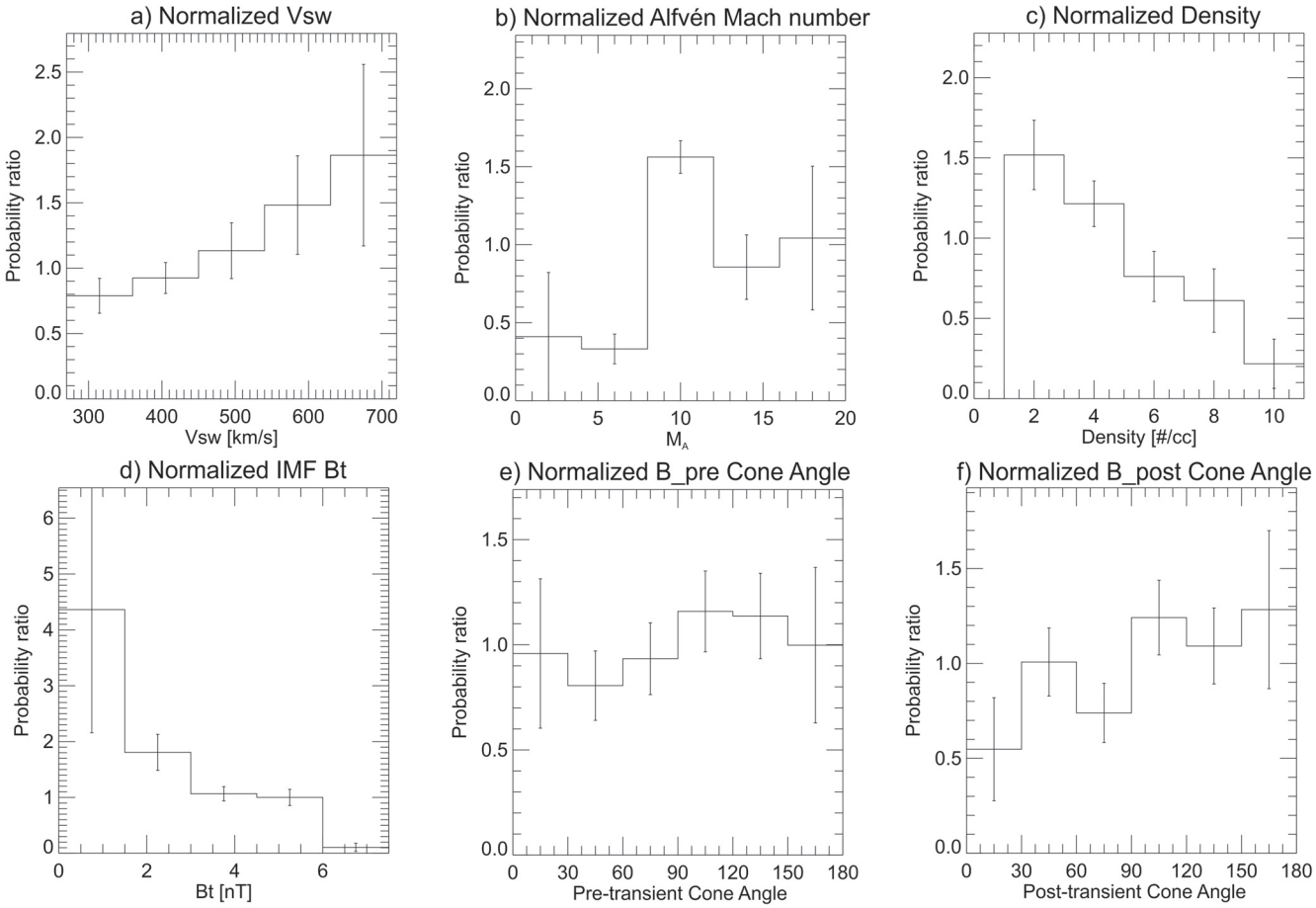

Figure 6. The probability distribution of solar wind parameters normalized by that from OMNI data (2010–2019): (a) solar wind speed, (b) solar wind Alfvén Mach number, (c) solar wind density, (d) IMF strength, (e) IMF cone angle before the events, and (f) IMF cone angle after the events.

with a shear angle less than 20° or 10°, respectively, which may be SHFAs or foreshock cavitons. Figure 8b shows that the angle between the TD normal and GSE-X direction (TD cone angle) does not affect the formation. This is different from the dayside statistical study by Schwartz et al. (2000) and Facskó, Németh, et al. (2009) showing a preference for large TD cone angles. The reason is likely because when the TD surface is more along the local bow shock normal, foreshock transients can more easily form. Thus, around the bow shock nose, along the bow shock normal means a large TD cone angle. However, in addition to the same reason as no correlation between IMF cone angles and θ_{Bn} of the midtail bow shock, midtail foreshock transients can form with a wide range of the bow shock normal from dayside to midtail and propagate to the spacecraft with the driver TD. Thus, there is no preferred TD cone angles shown in Figure 8b.

Figure 8c shows that the angle between the TD normal and the local bow shock normal is mainly within 90° ± 60°, indicating that the TD surface tends to be along the local bow shock normal consistent with Schwartz et al. (2000). Such an angle range can cover the angle variation of the bow shock normal from the nose to the flank (~60°). When the TD surface is along the dayside bow shock normal, the transit speed of the TD along the bow shock surface can be very small (V_{tr}) compared to the gyrospeed of reflected ions (V_g) so that the foreshock ions have sufficient time to interact with the TD (Schwartz et al., 2000). The ratio $V_{tr} / V_g = \cos\theta_{cs:sw} / 2\cos\theta_{bs:sw} \sin\theta_{Bn} \sin\theta_{cs:bs}$ is below 0.5 for most of events in Schwartz et al. (2000), where $\theta_{cs:sw}$ is the angle between TD normal and the solar wind (TD cone angle), $\theta_{bs:sw}$ is the angle between the bow shock normal and the solar wind, and $\theta_{cs:bs}$ is the angle between TD normal and the bow shock normal. However, this explanation only works around the nose of the bow shock where $\theta_{bs:sw}$ is small (~0°) and $\theta_{cs:sw}$ is large. On the flank with similar θ_{Bn} and $\theta_{cs:bs}$ but very large $\theta_{bs:sw}$ (~60°) and no preference to large $\theta_{cs:sw}$ (Figure 8b), more than half of events have ratio V_{tr} / V_g larger than 1 as shown in Figure 8d. A

21699402, 2021, 5, Downloaded from https://agupubs.onlinelibrary.wiley.com/doi/10.1029/2021JA029156 by Auburn University Libraries, Wiley Online Library on [08/11/2022]. See the Terms and Conditions (https://onlinelibrary.wiley.com/terms-and-conditions) on Wiley Online Library for rules of use; OA articles are governed by the applicable Creative Commons License

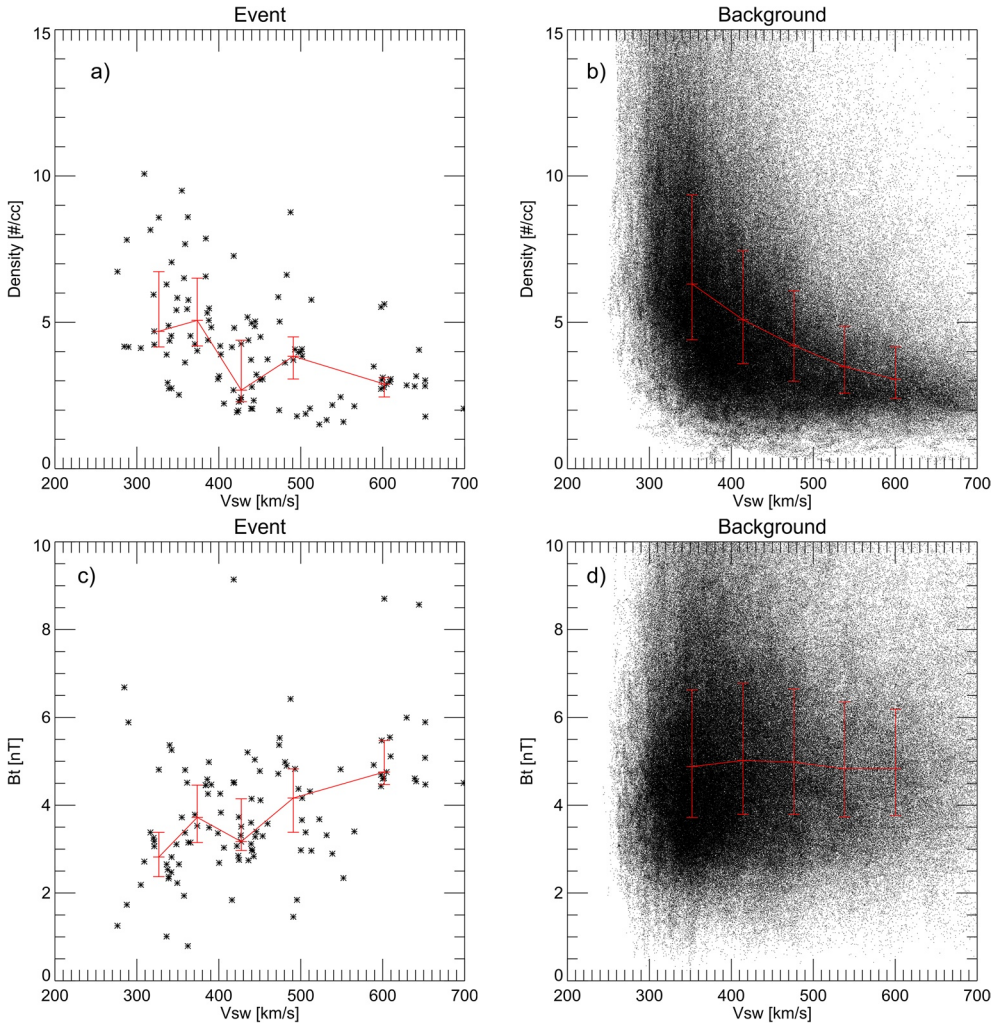

Figure 7. The relationship between the solar wind density and the solar wind speed for (a) each event and (b) from OMNI data. The relationship between the IMF strength and the solar wind speed for (c) each event and (d) from OMNI data. The red bars indicate the median value, upper quartile (75%), and lower quartile (25%).

possible explanation of this speed ratio difference is that because of the large curvature at the bow shock nose, the quasi-parallel region has a limited spatial range. Therefore, the TD has to move slowly along the bow shock surface so that it can stay longer in the foreshock to form foreshock transients. On the flank, on the other hand, the bow shock normal variation is very small, and the spatial scale of the foreshock region in the tailward direction can be very large, for example, more than 50 R_E. Thus, TDs in the midtail foreshock do not need to move slowly as in the dayside foreshock in order to have sufficient time to form foreshock transients. Therefore, there needs to be another reason why the TD surface tends to be along the local bow shock normal for foreshock transient formation.

Using the transit speed past the observation point and the event duration, we estimated that the spatial scale of midtail foreshock transients ranges from ~0.2 to 10 R_E with a median value of ~4 R_E (see probability distribution in Figure S4 in the supporting information). We do not see any strong correlation between the spatial scale and the solar wind speed or the distance along the bow shock surface (not shown). As the spatial scale of foreshock transients highly depends on the relative trajectory with which the spacecraft passes through the structure since foreshock transients have a complicated 3-D shape (e.g., T. Z. Liu et al., 2016b; 2017c), we do not perform further analysis on it.

21699402, 2021, 5, Downloaded from https://agupubs.onlinelibrary.wiley.com/doi/10.1029/2021JA029156 by Auburn University Libraries, Wiley Online Library on [08/11/2022]. See the Terms and Conditions (https://onlinelibrary.wiley.com/terms-and-conditions) on Wiley Online Library for rules of use; OA articles are governed by the applicable Creative Commons License

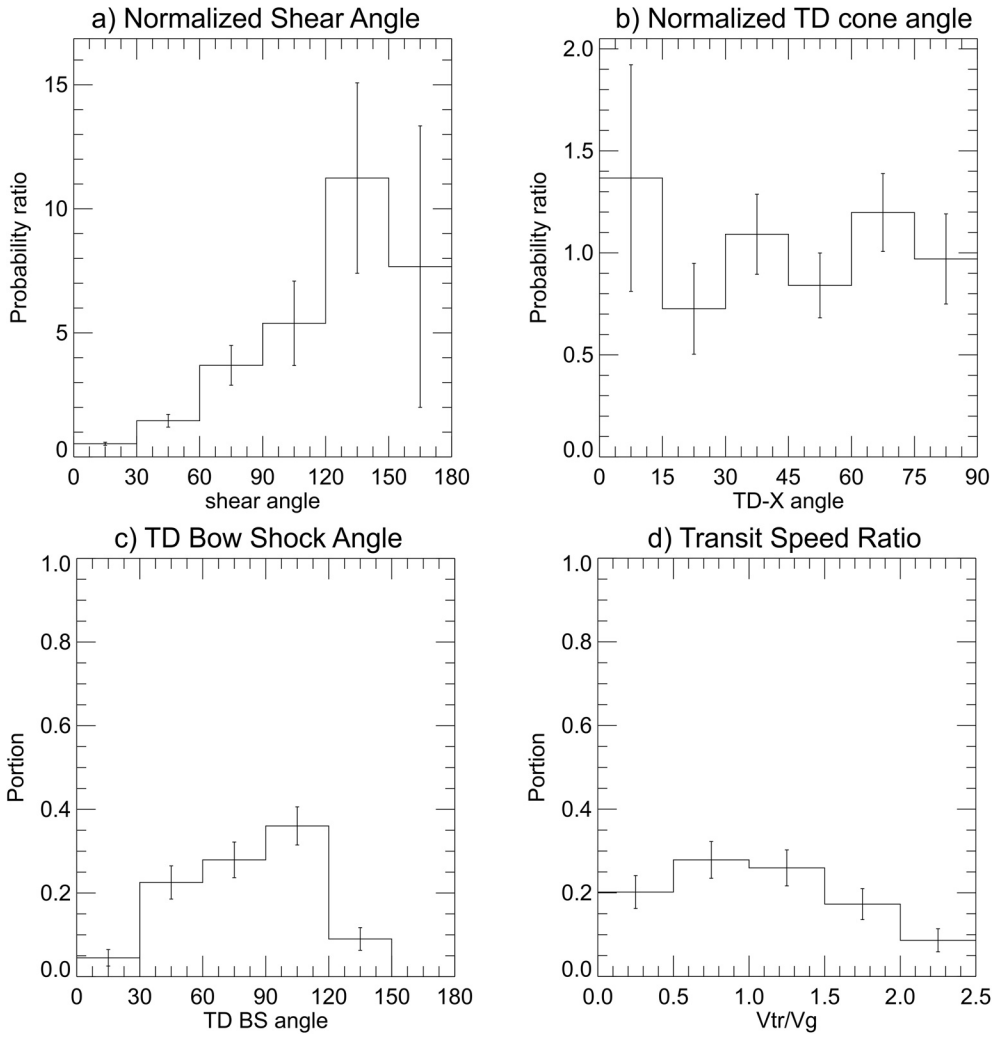

Figure 8. (a) The probability distribution of magnetic field shear angle across events normalized by the probability distribution of magnetic shear angle across solar wind TDs from ARTEMIS data (2010–2019). (b) Same format as (a) for the angle between the TD normal and GSE-X (from 0° to 90° as TD normal has 180° ambiguity unlike IMF). (c) The probability distribution of angle between the TD normal and the local bow shock normal (from the Merka et al. (2005) model). (d) The probability distribution of the transit speed of TDs along the bow shock surface (V_{tr}) divided by the gyrospeed of reflected ions (V_g) (Schwartz, Paschmann, et al., 2000).

We also compared whether the convection electric field points inward toward the discontinuity on one or both sides (a necessary condition for HFAs (e.g., Schwartz et al., 2000)). We found that there are 78 events (out of 111, ~70.2%) that have electric field pointing inward on one side, 22 events (~19.8%) on both sides, and 11 events (~9.9%) on neither side. Among the 11 events, 9 of them are likely foreshock cavities that do not require an electric field to point inward for their formation, but there are still two events which could be HFAs. A statistical study by S. Wang et al. (2013b) also showed that a few HFAs have electric field pointing outward on their two sides. Further investigation of the formation mechanisms is therefore needed (such as considering the kinetic effects of foreshock ions (T. Z. Liu et al., 2020a)).

4. Conclusions and Discussion

Using ARTEMIS observations, we conducted a statistical study of 111 midtail foreshock transients that have dynamic pressure along the local bow shock normal decrease by more than 50%, capable of disturbing the nightside bow shock and magnetosheath (e.g., T. Z. Liu et al., 2020c). We show that both density depletion and normal speed decrease contribute to the dynamic pressure decrease. Faster solar wind can result in

21699402, 2021, 5, Downloaded from https://agupubs.onlinelibrary.wiley.com/doi/10.1029/2021JA029156 by Auburn University Libraries, Wiley Online Library on [08/11/2022]. See the Terms and Conditions (https://onlinelibrary.wiley.com/terms-and-conditions) on Wiley Online Library for rules of use; OA articles are governed by the applicable Creative Commons License

21699402, 2021, 5, Downloaded from https://agupubs.onlinelibrary.wiley.com/doi/10.1029/2021JA029156 by Auburn University Libraries, Wiley Online Library on [08/11/2022]. See the Terms and Conditions (https://onlinelibrary.wiley.com/terms-and-conditions) on Wiley Online Library for rules of use; OA articles are governed by the applicable Creative Commons License

larger normal speed decrease and favors stronger dynamic pressure decrease. Most events show electron heating, which is proportional to the solar wind speed. The dynamic pressure depletion and electron heating are independent of the tailward distance along the bow shock surface and are likely more significant when the events are closer to the bow shock. The dynamic pressure decrease and the electron heating are correlated. As for the solar wind conditions, we show that foreshock transients occur preferentially under larger solar wind speed and lower IMF strength. Large Mach number is also a favorable condition. However, contrary to dayside foreshock transients, IMF and TD cone angles do not appear to affect formation, though the IMF direction and TD surface do tend to be along the local bow shock normal, same as in the dayside. The ratio of TD transit speed to the gyrospeed of reflected ions do not need to be small.

The midtail foreshock transients typically have weaker velocity variation in the core than dayside HFAs, SHFAs, and FBs. As weak or strong velocity variation is one critical criterion to categorize foreshock transients, some midtail foreshock transients may be misidentified as foreshock cavities or foreshock cavitons. There are multiple reasons for the misidentification. First, for the same decrease ratio of speed along the local bow shock normal and the same solar wind speed, the magnitude of the velocity variation at the midtail bow shock is only around half of that at the bow shock nose. For example, if we look at Figure 1a, the velocity in the core only shows a very small variation compared to the background. We may identify it as a foreshock cavity based on experience from dayside observations. However, the normal speed ratio in this event is ~60%. In other words, if we plot this event in the shock normal incidence frame (NIF), we will see very clear decrease in normal speed component, indicating an HFA (Figure S5). The spacecraft rest frame is very close to NIF in the dayside observations but very different at midtail. Therefore, transformation to a universal reference frame (e.g., NIF) instead of the spacecraft rest frame is necessary before any comparison of observed velocities. As shown in Figure S6, the deflection angle in NIF is mostly below 15° (82 out of 111), indicating that most events have mainly normal speed deceleration (e.g., Figure S5) while the rest also exhibit a clear deflection in the tangential direction (with deflection angle up to ~90°). In comparison, the maximum deflection angle in the spacecraft rest frame is ~30° (Figure 2e) governed by the tilted bow shock normal and strong solar wind tangential component. A second reason for the misidentification may be that the local Mach number is around half of that at the nose, so the contribution to deflection and deceleration from the presence of foreshock ions could be weak. This means that even though the formation process is consistent with HFAs, FBs, or SHFAs, the relatively weak velocity variation due to low Mach number compared to the typical dayside bow shock could make them categorized as foreshock cavities or foreshock cavitons.

Based on whether the normal speed ratio (which has same values in any bow shock rest frames, e.g., Earth's rest frame, NIF, and de Hoffmann-Teller frame) is larger or smaller than 0.8 and whether the magnetic shear angle is larger or smaller than 15°, we determined that there are 46 HFAs or FBs, 12 SHFAs, 43 foreshock cavities, and 10 foreshock cavitons in our database. Had we required that there be only a shock at the trailing boundary, there would have been 3 FBs out of the 46. Different types of foreshock transients have markedly different properties. For example, HFAs, SHFAs, and FBs show stronger dynamic pressure decrease and electron heating than foreshock cavities and foreshock cavitons (Figure S7). In the group of "close to the bow shock" (Figures 5c and 5d), 45 out of 68 events are HFAs, SHFAs, or FBs, whereas only 13 of them (out of 43) are in the group of "far away from the bow shock". This together with Figure S7 contributes to the differences of probability distributions between the two groups shown in Figures 5c and 5d. Among the events that were observed by both spacecraft, foreshock cavities are the dominant type, likely because their sizes are typically larger than the other types, especially along the bow shock normal direction (the two spacecraft were often separated by a few R_E along this direction). These results are similar to those at the dayside.

Our results also indicate that some foreshock transients may not be "transient". At the nose of the bow shock where the curvature is strong, foreshock transients may soon disappear after they propagate out from the quasi-parallel regime. At the bow shock flanks, however, the bow shock normal varies only quite gradually, so that the foreshock region can be very large compared to the dayside. Some foreshock transients could appear stable while propagating tailward along the nightside bow shock as suggested by Figure 5 (if most foreshock transients dissipate, the spacecraft further downtail will more likely observe weaker perturbations) and the case study by T. Z. Liu et al. (2020c). Simulations by C.-P. Wang, Wang, et al. (2020) also

show that an FB propagates from dayside to midtail and does not dissipate. Our results imply that foreshock transients at planar shocks can exist for a considerably long time (depending on the shock scales, e.g., tens of minutes on Earth's bow shock flanks and much longer on Saturn's bow shock flanks). Our results also show that almost all foreshock transients in the midtail foreshock heat electrons. The case study by T. Z. Liu et al. (2020c) also showed ion heating. Such heating does not clearly dissipate during tailward propagation (Figure 5 and the case study by T. Z. Liu et al. (2020c)). This implies that foreshock transients have to continuously heat/energize particles, as energetic particles can leak out (e.g., T. Z. Liu et al., 2017c). Therefore, our results imply that at planar shocks, foreshock transients could continuously disturb the local shock and contribute to local particle heating/energization for a very long time (e.g., tens of minutes).

Additionally, some formation conditions of foreshock transients based on dayside observations are limited by the dayside bow shock geometry. Our results indicate that the formation conditions concerning IMF direction, TD orientation, and the transit speed of TDs have to be revisited for midtail foreshock transients. Therefore, both the observational properties and formation conditions of foreshock transients need to be generalized in order to identify them in other shock environments, for example, other planetary bow shocks with smaller or larger Mach numbers, large-scale planar or very curved shocks, and shocks that are not observed in the shock NIF.

Data Availability Statement

The ARTEMIS data and THEMIS software (TDAS, a SPEDAS v3.1 plugin, see Angelopoulos et al. (2019)) are available at http://themis.ssl.berkeley.edu. OMNI data are available at CDAWeb (http://cdaweb.gsfc.nasa.gov/).

Acknowledgments
T. Z. L. is supported by the NASA Living With a Star Jack Eddy Postdoctoral Fellowship Program, administered by the Cooperative Programs for the Advancement of Earth System Science (CPAESS). T. Z. L. is partially supported by NSF award AGS-1941012. H. Z. is partially supported by NSF AGS-1352669. C.-P. Wang is supported by NASA 80NSSC19K0840. We thank the SPEDAS software team and NASA's Coordinated Data Analysis Web (CDAWeb, http://cdaweb.gsfc.nasa.gov/) for their analysis tools and data access.

References

An, X., Liu, T. Z., Bortnik, J., Osmane, A., & Angelopoulos, V. (2020). Formation of foreshock transients and associated secondary shocks. *The Astrophysical Journal*, *901*(1), 73. https://doi.org/10.3847/1538-4357/abaf03

Angelopoulos, V. (2008). The THEMIS mission. *Space Science Reviews*, *141*, 5–34. https://doi.org/10.1007/s11214-008-9336-1

Angelopoulos, V., Cruce, P., Drozdov, A., Grimes, E. W., Hatzigeorgiu, N., King, D. A., et al. (2019). The space physics environment data analysis system (SPEDAS). *Space Science Reviews*, *215*, 9. https://doi.org/10.1007/s11214-018-0576-4

Archer, M. O., Turner, D. L., Eastwood, J. P., Horbury, T. S., & Schwartz, S. J. (2014). The role of pressure gradients in driving sunward magnetosheath flows and magnetopause motion. *Journal of Geophysical Research: Space Physics*, *119*, 8117–8125. https://doi.org/10.1002/2014JA020342

Archer, M. O., Turner, D. L., Eastwood, J. P., Schwartz, S. J., & Horbury, T. S. (2015). Global impacts of a foreshock bubble: Magnetosheath, magnetopause and ground-based observations. *Planetary and Space Science*, *106*, 56–66. https://doi.org/10.1016/j.pss.2014.11.026

Auster, H. U., Glassmeier, K. H., Magnes, W., Aydogar, O., Baumjohann, W., Constantinescu, D., et al. (2008). The THEMIS fluxgate magnetometer. *Space Science Reviews*, *141*, 235–264. https://doi.org/10.1007/s11214-008-9365-9

Blanco-Cano, X., Kajdič, P., Omidi, N., & Russell, C. T. (2011). Foreshock cavitons for different interplanetary magnetic field geometries: Simulations and observations. *Journal of Geophysical Research*, *116*, A09101. https://doi.org/10.1029/2010JA016413

Blanco-Cano, X., Omidi, N., & Russell, C. T. (2009). Global hybrid simulations: Foreshock waves and cavitons under radial interplanetary magnetic field geometry. *Journal of Geophysical Research*, *114*, A01216. https://doi.org/10.1029/2008JA013406

Chu, C., Zhang, H., Sibeck, D., Otto, A., Zong, Q., Omidi, N., et al. (2017). THEMIS satellite observations of hot flow anomalies at Earth's bow shock. *Annales Geophysicae*, *35*(3), 443–451. https://doi.org/10.5194/angeo-35-443-2017

Eastwood, J. P., Lucek, E. A., Mazelle, C., Meziane, K., Narita, Y., Pickett, J., & Treumann, R. A. (2005). The foreshock. *Space Science Reviews*, *118*, 41–94. https://doi.org/10.1007/s11214-005-3824-3

Facskó, G., Németh, Z., Erdős, G., Kis, A., & Dandouras, I. (2009). A global study of hot flow anomalies using cluster multi-spacecraft measurements. *Annales Geophysicae*, *27*(5), 2057–2076. https://doi.org/10.5194/angeo-27-2057-2009

Facskó, G., Opitz, A., Lavraud, B., Luhmann, J. G., Russell, C. T., Sauvaud, J.-A., et al. (2015). Hot flow anomaly remnant in the far geotail?. *Journal of Atmospheric and Solar-Terrestrial Physics*, *124*, 39–43. https://doi.org/10.1016/j.jastp.2015.01.011

Greco, A., Chuychai, P., Matthaeus, W. H., Servidio, S., & Dmitruk, P. (2008). Intermittent MHD structures and classical discontinuities. *Geophysical Research Letters*. https://doi.org/10.1029/2008GL035454

Kis, A., Agapitov, O., Krasnoselskikh, V., Khotyaintsev, Y. V., Dandouras, I., Lemperger, I., & Wesztergom, V. (2013). Gyrosurfing acceleration of ions in front of Earth's quasi-parallel bow shock. *The Astrophysical Journal*, *771*, 4. https://doi.org/10.1088/0004-637X/771/1/4

Lin, Y. (1997). Generation of anomalous flows near the bow shock by its interaction with interplanetary discontinuities. *Journal of Geophysical Research*, *102*(A11), 24265–24281. https://doi.org/10.1029/97JA01989

Lin, Y. (2002). Global hybrid simulation of hot flow anomalies near the bow shock and in the magnetosheath. *Planetary and Space Science*, *50*, 577–591. https://doi.org/10.1016/s0032-0633(02)00037-5

Liu, T. Z., An, X., Zhang, H., & Turner, D. (2020). Magnetospheric multiscale (MMS) observations of foreshock transients at their very early stage. *The Astrophysical Journal*, *902*(1), 5. https://doi.org/10.3847/1538-4357/abb249

Liu, T. Z., Angelopoulos, V., & Hietala, H. (2017). Energetic ion leakage from foreshock transient cores. *Journal of Geophysical Research: Space Physics*, *122*, 7209–7225. https://doi.org/10.1002/2017JA024257

Liu, T. Z., Angelopoulos, V., Hietala, H., & Wilson, L. B., III. (2017). Statistical study of particle acceleration in the core of foreshock transients. *Journal of Geophysical Research: Space Physics*, *122*, 7197–7208. https://doi.org/10.1002/2017JA024043

21699402, 2021, 5, Downloaded from https://agupubs.onlinelibrary.wiley.com/doi/10.1029/2021JA029156 by Auburn University Libraries, Wiley Online Library on [08/11/2022]. See the Terms and Conditions (https://onlinelibrary.wiley.com/terms-and-conditions) on Wiley Online Library for rules of use; OA articles are governed by the applicable Creative Commons License

Liu, T. Z., Angelopoulos, V., & Lu, S. (2019). Relativistic electrons generated at Earth's quasi-parallel bow shock. *Science Advances*, *5*(7), eaaw1368. https://doi.org/10.1126/sciadv.aaw1368

Liu, T. Z., Hietala, H., Angelopoulos, V., & Turner, D. L. (2016). Observations of a new foreshock region upstream of a foreshock bubble's shock. *Geophysical Research Letters*, *43*, 4708–4715. https://doi.org/10.1002/2016GL068984

Liu, T. Z., Lu, S., Angelopoulos, V., Hietala, H., & Wilson, L. B., III. (2017b). Fermi acceleration of electrons inside foreshock transient cores. *Journal of Geophysical Research: Space Physics*, *122*, 9248–9263. https://doi.org/10.1002/2017JA024480

Liu, T. Z., Lu, S., Angelopoulos, V., Lin, Y., & Wang, X. Y. (2018). Ion acceleration inside foreshock transients. *Journal of Geophysical Research: Space Physics*, *123*, 163–178. https://doi.org/10.1002/2017JA024838

Liu, T. Z., Lu, S., Turner, D. L., Gingell, I., Angelopoulos, V., Zhang, H., et al. (2020). Magnetospheric multiscale (MMS) observations of magnetic reconnection in foreshock transients. *Journal of Geophysical Research: Space Physics*, *125*, e2020JA027822. https://doi.org/10.1029/2020JA027822

Liu, T. Z., Turner, D. L., Angelopoulos, V., & Omidi, N. (2016). Multipoint observations of the structure and evolution of foreshock bubbles and their relation to hot flow anomalies. *Journal of Geophysical Research: Space Physics*, *121*, 5489. https://doi.org/10.1002/2016JA022461

Liu, T. Z., Wang, C.-P., Wang, B., Wang, X., Zhang, H., Lin, Y., et al. (2020). ARTEMIS observations of foreshock transients in the midtail foreshock. *Geophysical Research Letters*, *47*, e2020GL090393. https://doi.org/10.1029/2020GL090393

Liu, Z., Turner, D. L., Angelopoulos, V., & Omidi, N. (2015). THEMIS observations of tangential discontinuity-driven foreshock bubbles. *Geophysical Research Letters*, *42*, 7860–7866. https://doi.org/10.1002/2015GL065842

McFadden, J. P., Carlson, C. W., Larson, D., Ludlam, M., Abiad, R., Elliott, B., et al. (2008). The THEMIS ESA plasma instrument and in-flight calibration. *Space Science Reviews*, *141*, 277–302. https://doi.org/10.1007/s11214-008-9440-2

Merka, J., Szabo, A., Slavin, J. A., & Peredo, M. (2005). Three-dimensional position and shape of the bow shock and their variation with upstream Mach numbers and interplanetary magnetic field orientation. *Journal of Geophysical Research*, *110*, A04202. https://doi.org/10.1029/2004JA010944

Omidi, N., Eastwood, J. P., & Sibeck, D. G. (2010). Foreshock bubbles and their global magnetospheric impacts. *Journal of Geophysical Research*, *115*, A06204. https://doi.org/10.1029/2009JA014828

Omidi, N., Lee, S. H., Sibeck, D. G., Turner, D. L., Liu, T. Z., & Angelopoulos, V. (2020). Formation and topology of foreshock bubbles. *Journal of Geophysical Research: Space Physics*, *125*, e2020JA028058. https://doi.org/10.1029/2020JA028058

Omidi, N., Sibeck, D., Blanco-Cano, X., Rojas-Castillo, D., Turner, D., Zhang, H., & Kajdič, P. (2013). Dynamics of the foreshock compressional boundary and its connection to foreshock cavities. *Journal of Geophysical Research: Space Physics*, *118*, 823–831. https://doi.org/10.1002/jgra.50146

Omidi, N., & Sibeck, D. G. (2007). Formation of hot flow anomalies and solitary shocks. *Journal of Geophysical Research*, *112*, A10203. https://doi.org/10.1029/2006JA011663

Omidi, N., Zhang, H., Sibeck, D., & Turner, D. (2013). Spontaneous hot flow anomalies at quasi-parallel shocks: 2. Hybrid simulations. *Journal of Geophysical Research: Space Physics*, *118*, 173–180. https://doi.org/10.1029/2012JA018099

Paschmann, G., & Sckopke, N. (1983). Ion reflection and heating at the Earth's bow shock. In G. Haerendel, & B. Battrick (Eds.), Eds., *Topics in plasma-, astro-, and space physics: A volume dedicated to Reimar Lüst* (pp. 139–146). Garching: MPE.

Russell, C. T. (1985). Planetary bow shocks. In B. T. Tsurutani, & R. G. Stone (Eds.), Eds., *Collisionless shocks in the heliosphere: Reviews of current research*. https://doi.org/10.1029/GM035p0109

Šafránková, J., Přech, L., Němeček, Z., & Sibeck, D. G. (2002). The structure of hot flow anomalies in the magnetosheath. *Advances in Space Research*, *30*, 2737–2744.

Schwartz, S. J. (1998). In G. Paschmann, & P. W. Daly (Eds.), Eds., *Shock and discontinuity normal, Mach numbers, and related parameters, from analysis methods for multi-spacecraft data* (pp. 249–270).

Schwartz, S. J., Avanov, L., Turner, D., Zhang, H., Gingell, I., Eastwood, J. P., et al. (2018). Ion kinetics in a hot flow anomaly: MMS observations. *Geophysical Research Letters*, *45*(21), 11520–11529. https://doi.org/10.1029/2018GL080189

Schwartz, S. J., Chaloner, C. P., Christiansen, P. J., Coates, A. J., Hall, D. S., Johnstone, A. D., et al. (1985). An active current sheet in the solar wind. *Nature*, *318*, 269–271. https://doi.org/10.1038/318269a0

Schwartz, S. J., Paschmann, G., Sckopke, N., Bauer, T. M., Dunlop, M., Fazakerley, A. N., & Thomsen, M. F. (2000). Conditions for the formation of hot flow anomalies at Earth's bow shock. *Journal of Geophysical Research*, *105*(A6), 12639–12650. https://doi.org/10.1029/1999JA000320

Shen, X.-C., Shi, Q., Wang, B., Zhang, H., Hudson, M. K., Nishimura, Y., et al. (2018). Dayside magnetospheric and ionospheric responses to a foreshock transient on 25 June 2008: 1. FLR observed by satellite and ground-based magnetometers. *Journal of Geophysical Research: Space Physics*, *123*, 6335–6346. https://doi.org/10.1029/2018JA025349

Sibeck, D. G., Borodkova, N. L., Schwartz, S. J., Owen, C. J., Kessel, R., Kokubun, S., et al. (1999). Comprehensive study of the magnetospheric response to a hot flow anomaly. *Journal of Geophysical Research*, *104*(A3), 4577–4593. https://doi.org/10.1029/1998JA900021

Sibeck, D. G., Phan, T. D., Lin, R. P., Lepping, R. P., & Szabo, A. (2002). Wind observations of foreshock cavities: A case study. *Journal of Geophysical Research*, *107*(A10), 1271. https://doi.org/10.1029/2001JA007539

Turner, D. L., Eriksson, S., Phan, T. D., Angelopoulos, V., Tu, W., Liu, W., et al. (2011). Multispacecraft observations of a foreshock-induced magnetopause disturbance exhibiting distinct plasma flows and an intense density compression. *Journal of Geophysical Research*, *116*, A04230. https://doi.org/10.1029/2010JA015668

Turner, D. L., Liu, T. Z., Wilson, L. B., Cohen, I. J., Gershman, D. G., Fennell, J. F., et al. (2020). Microscopic, multipoint characterization of foreshock bubbles with magnetospheric multiscale (MMS). *Journal of Geophysical Research: Space Physics*, *125*, e2019JA027707. https://doi.org/10.1029/2019JA027707

Turner, D. L., Omidi, N., Sibeck, D. G., & Angelopoulos, V. (2013). First observations of foreshock bubbles upstream of Earth's bow shock: Characteristics and comparisons to HFAs. *Journal of Geophysical Research Space Physics*, *118*, 1552–1570. https://doi.org/10.1002/jgra.50198

Turner, D. L., Wilson, L. B., Liu, T. Z., Cohen, I. J., Schwartz, S. J., Osmane, A., et al. (2018). Autogenous and efficient acceleration of energetic ions upstream of Earth's bow shock. *Nature*, *561*, 206. https://doi.org/10.1038/s41586-018-0472-9

Wang, B., Liu, T., Nishimura, Y., Zhang, H., Hartinger, M., Shi, X., et al. (2020). Global propagation of magnetospheric Pc5 ULF waves driven by foreshock transients. *Journal of Geophysical Research: Space Physics*, *125*, e2020JA028411. https://doi.org/10.1029/2020JA028411

Wang, B., Nishimura, Y., Hietala, H., Shen, X.-C., Shi, X.-C., Zhang, H., et al. (2018). Dayside magnetospheric and ionospheric responses to a foreshock transient on 25 June 2008: 2. 2-D evolution based on dayside auroral imaging. *Journal of Geophysical Research: Space Physics*, *123*, 6347–6359. https://doi.org/10.1029/2017JA024846

21699402, 2021, 5, Downloaded from https://agupubs.onlinelibrary.wiley.com/doi/10.1029/2021JA029156 by Auburn University Libraries, Wiley Online Library on [08/11/2022]. See the Terms and Conditions (https://onlinelibrary.wiley.com/terms-and-conditions) on Wiley Online Library for rules of use; OA articles are governed by the applicable Creative Commons License

Wang, C.-P., Liu, T. Z., Xing, X., & Masson, A. (2018). Multispacecraft observations of tailward propagation of transient foreshock perturbations to midtail magnetosheath. *Journal of Geophysical Research: Space Physics*, *123*, 9381–9394. https://doi.org/10.1029/2018JA025921

Wang, C.-P., Wang, X., Liu, T. Z., & Lin, Y. (2020). Evolution of a foreshock bubble in the midtail foreshock and impact on the magnetopause: 3D global hybrid simulation. *Geophysical Research Letters*, *47*, e2020GL089844. https://doi.org/10.1029/2020GL089844

Wang, S., Chen, L.-J., Bessho, N., Hesse, M., Wilson, L. B., Denton, R., et al. (2020). Ion-scale current structures in short large-amplitude magnetic structures. *The Astrophysical Journal*, *898*(121), 121. https://doi.org/10.3847/1538-4357/ab9b8b

Wang, S., Zong, Q., & Zhang, H. (2013a). Cluster observations of hot flow anomalies with large flow deflections: 1. Velocity deflections. *Journal of Geophysical Research: Space Physics*, *118*, 732–743. https://doi.org/10.1002/jgra.50100

Wang, S., Zong, Q., & Zhang, H. (2013b). Hot flow anomaly formation and evolution: Cluster observations. *Journal of Geophysical Research: Space Physics*, *118*, 4360–4380. https://doi.org/10.1002/jgra.50424

Wilson, L. B., III, Koval, A., Sibeck, D. G., Szabo, A., Cattell, C. A., Kasper, J. C., et al. (2013). Shocklets, SLAMS, and field-aligned ion beams in the terrestrial foreshock. *Journal of Geophysical Research: Space Physics*, *118*, 957–966. https://doi.org/10.1029/2012JA018186

Wilson, L. B. II. I, Sibeck, D. G., Turner, D. L., Osmane, A., Caprioli, D., & Angelopoulos, V. (2016). Relativistic electrons produced by foreshock disturbances observed upstream of Earth's bow shock. *Physical Review Letters*, *117*(21), 215101. https://doi.org/10.1103/PhysRevLett.117.215101

Zhang, H., Sibeck, D. G., Zong, Q.-G., Gary, S. P., McFadden, J. P., Larson, D., et al. (2010). Time history of events and macroscale interactions during substorms observations of a series of hot flow anomaly events. *Journal of Geophysical Research*, *115*, A12235. https://doi.org/10.1029/2009JA015180

Zhang, H., Sibeck, D. G., Zong, Q.-G., Omidi, N., Turner, D., & Clausen, L. B. N. (2013). Spontaneous hot flow anomalies at quasi-parallel shocks: 1. Observations. *Journal of Geophysical Research: Space Physics*, *118*, 3357–3363. https://doi.org/10.1002/jgra.50376

Zhao, L. L., Zhang, H., & Zong, Q. G. (2017a). Global ULF waves generated by a hot flow anomaly. *Geophysical Research Letters*, *44*, 5283–5291. https://doi.org/10.1002/2017GL073249

Zhao, L. L., Zhang, H., & Zong, Q. G. (2017b). A statistical study on hot flow anomaly current sheets. *Journal of Geophysical Research: Space Physics*, *122*, 235–248. https://doi.org/10.1002/2016JA023319

21699402, 2021, 5, Downloaded from https://agupubs.onlinelibrary.wiley.com/doi/10.1029/2021JA029156 by Auburn University Libraries, Wiley Online Library on [08/11/2022]. See the Terms and Conditions (https://onlinelibrary.wiley.com/terms-and-conditions) on Wiley Online Library for rules of use; OA articles are governed by the applicable Creative Commons License